



Cite this: *Phys. Chem. Chem. Phys.*,
2023, 25, 17860

ONIOM meets *xtb*: efficient, accurate, and robust multi-layer simulations across the periodic table[†]

Christoph Plett, ^a Abylay Katbashev, ^a Sebastian Ehlert, ^b Stefan Grimme ^a* and Markus Bursch ^c

The computational treatment of large molecular structures is of increasing interest in fields of modern chemistry. Accordingly, efficient quantum chemical approaches are needed to perform sophisticated investigations on such systems. This engaged the development of the well-established “Our own N-layered integrated molecular orbital and molecular mechanics” (ONIOM) multi-layer scheme [L. W. Chung *et al.*, *Chem. Rev.*, 2015, **115**, 5678–5796]. In this work, we present the specific implementation of the ONIOM scheme into the *xtb* semi-empirical extended tight-binding program package and its application to challenging transition-metal complexes. The efficient and broadly applicable GFN_n-*xtb* and -FF methods are applied in the ONIOM framework to elucidate reaction energies, geometry optimizations, and explicit solvation effects for metal–organic systems with up to several hundreds of atoms. It is shown that an ONIOM-based combination of density functional theory, semi-empirical, and force-field methods can be used to drastically reduce the computational costs and thus enable the investigation of huge systems at almost no significant loss in accuracy.

Received 12th May 2023,
Accepted 22nd June 2023

DOI: 10.1039/d3cp02178e

rsc.li/pccp

1 Introduction

Current developments and modern techniques for synthesizing and analyzing molecules allow chemists to study increasingly large and complex systems including, *e.g.*, macromolecules, reaction networks, or supramolecular complexes.^{1–3} Besides a long-standing emphasis on protein structures and their functions in the macro-molecular regime,⁴ large metal–organic structures such as metal–organic polyhedra (MOP)^{5,6} or molecular machines^{7,8} gain growing attention and find application in various fields like drug-delivery processes,^{9,10} functional materials,¹¹ catalysis,^{12,13} or fuel storage.¹⁴ Such systems can also reach impressive sizes of hundreds to thousands of atoms and may involve moieties with challenging electronic structures. Besides advancing experimental techniques, computational methods and workflows became a valuable utility for a reliable description of large molecular systems enabling deeper insights into basic properties and mechanisms.^{15,16} However, the application of accurate quantum chemical (QC) methods like density functional theory (DFT) and wave function theory

(WFT) methods to extended systems is often limited due to the rapidly increasing computational costs with the system size.¹⁷

This encouraged the continuous development of force field (FF) and semi-empirical quantum mechanical (SQM) methods that are routinely applied to systems of hundreds up to thousands of atoms.^{18–21} More recent developments in this field are the GFN_n-*xtb* and force-field methods,²² GFN1-xTB,²³ GFN2-xTB,²⁴ and GFN-FF,²⁵ which became widely used and well-established tools for the treatment of large systems.^{26,27} In contrast to most other semi-empirical approaches and FFs, the GFN methods are consistently parameterized for all elements up to Rn and are thus applicable to a large chemical space throughout the periodic table. These methods are already routinely used in black-box approaches for conformer sampling,²⁸ energetic sorting of structure ensembles,²⁹ or docking algorithms such as the recent aISS³⁰ method with the latter being well-suited for molecule-binding to large structures.¹⁴ Nevertheless, complex and challenging electronic structures often require an even more accurate direct or post-processing description at a more sophisticated DFT or WFT level.³¹

To close this gap, various multi-layer schemes have emerged. They rely on the fact that treating the whole system highly accurately is often unnecessary, but rather a small reactive part or interaction site is of importance.³² For multi-layer schemes, computationally demanding but accurate methods are applied only to a small region of interest while non-negligible environmental effects are treated with computationally cheaper methods. Crucial environmental influences include, *e.g.*, backbone

^a Mulliken Center for Theoretical Chemistry, Universität Bonn, Beringstr. 4, 53115 Bonn, Germany. E-mail: grimme@thch.uni-bonn.de

^b Microsoft Research AI4Science, Evert van de Bekkstraat 254, 1118 CZ Schiphol, The Netherlands

^c Max-Planck-Institut für Kohlenforschung, Kaiser-Wilhelm-Platz 1, 45470 Mülheim an der Ruhr, Germany. E-mail: bursch@kofo.mpg.de

† Electronic supplementary information (ESI) available. See DOI: <https://doi.org/10.1039/d3cp02178e>



strain in proteins,³³ supramolecular stabilization of reactive species,^{34,35} reaction mechanisms including large structurally strained systems,³⁶ or explicit solvation.^{37,38} Besides well-known QM/MM schemes,³⁹ the so-called “Our own *N*-layered integrated molecular orbital and molecular mechanics” (ONIOM) method^{32,40} proved to be a valuable tool for multi-layer simulations. ONIOM was already successfully applied for modeling organic reactions such as Friedel–Crafts reactions,⁴¹ metal–organic catalysis,⁴² and zeolite reactivity to only name a few.⁴³ In this context, the GFN methods represent a perfect match to simulate the outer region within the ONIOM scheme due to their broad parameterization and reasonable accuracy.^{19,44–46}

Accordingly, we present here the implementation of the ONIOM scheme in the open source *xtb* program that allows the direct combination of the GFN methods with any desired DFT or WFT method *via* an interface to the prominent ORCA^{47,48} or TURBOMOLE^{49,50} program packages in an easily applicable and intuitive way. This enables the efficient and accurate treatment of not only organic structures but also of molecules containing, *e.g.*, transition metals, heavy main group elements, or even lanthanoids.^{19,46} Besides the theoretical excursion into the ONIOM approach and its implementation in *xtb*, we demonstrate its efficient application by investigating molecular geometries and energies of challenging metal–organic structures.

2 Theoretical overview and implementation

In principle, multi-layer techniques used to intermix different levels of QC theory are either additive or subtractive. Additive schemes such as QM/MM or QM/QM were established first and rely on coupling terms between the two regions treated with different methods.^{51,52} Subtractive schemes like ONIOM do not require additional coupling terms in the Hamiltonian and are thus easier to implement and allow the straightforward mixing of any methods. For the simplest form of the ONIOM scheme, the whole system is divided into two layers: an inner and outer region. These regions are typically treated separately with a high- ($E_{\text{inner}}^{\text{high}}$) (*e.g.*, DFT) and low-level ($E_{\text{outer}}^{\text{low}}$) method (*e.g.*, SQM or FF) and consequently fused to obtain the ONIOM energy expression:

$$E_{\text{ONIOM}} = E_{\text{inner}}^{\text{high}} + E_{\text{outer}}^{\text{low}} \quad (1)$$

The low-level description of the outer region is obtained by the subtraction of the energy of the inner region ($E_{\text{inner}}^{\text{low}}$) from the energy of the whole system ($E_{\text{whole}}^{\text{low}}$) calculated with the corresponding low-level approach:

$$E_{\text{outer}}^{\text{low}} = E_{\text{whole}}^{\text{low}} - E_{\text{inner}}^{\text{low}} \quad (2)$$

In this implementation, no electrostatic embedding is employed for the calculation of the inner region.

If requested, solvation effects can be accounted for by a simplified solvation embedding. Thereby, only $E_{\text{whole}}^{\text{low}}$ is computed

embedded in an implicit solvent model while the inner region is always computed in the gas phase.

2.1 ONIOM boundary

The artificial separation of a chemical system into different regions and the creation of the corresponding boundaries between them can be challenging. The trivial case is to deal with boundaries that include only non-covalent interactions. In contrast, treating large molecules with a coupling scheme like ONIOM leads usually to covalent bond breaking. In such cases, the artificial partitioning of the system leads to the formation of radicals or dangling bonds at the boundaries. To address this problem, a number of different approaches were developed^{32,53} such as the link atom (LA) approach^{54,55} or the frozen localized orbitals⁵⁶ approach. Herein, we consider only the former, which is implemented within the *xTB* software in the course of this work.

The general idea behind the link atom saturation technique is the capping of the cleaved bonds to fill the incomplete valence shells of the interface atoms of the partitioned inner region. This is done *via* the introduction of a dummy atom, usually Hydrogen, on the bond vector between the boundary atoms. The exact position of a link atom is derived as:

$$\vec{R}_{\text{LA}} = \vec{R}_{\text{inner}} + k(\vec{R}_{\text{outer}} - \vec{R}_{\text{inner}}) \quad (3)$$

where \vec{R}_{inner} and \vec{R}_{outer} are the coordinates of the atoms in the inner and outer regions with mutual bonds, that split during the ONIOM procedure, and k is the distance scaling factor. Conventionally, k is taken as a constant determined from the predefined element-specific distances between the inner region atom (IA)–outer region atom (OA) and IA–H atoms listed in the ESI.† For cases without listed values, a default value for k is chosen as the ratio of the carbon–carbon/carbon–hydrogen bond distances. As an alternative, we implemented the possibility to make the scaling factor k dependent on the actual value of the IA–OA distance that is present in the system. The corresponding derivatives are given in the ESI.† Fig. 1 demonstrates the ONIOM interpolation scheme, where the chemical system is first partitioned by cleaving its C–C σ bonds, and then saturated with hydrogen atoms *via* the link atom approach.

2.2 Topology

One of the distinguishing features of the *xTB* ONIOM implementation is the usage of the topology information generated with the corresponding GFN method to automate and validate the partitioning and saturation. As cutting double or triple bonds can lead to problematic systems, *xTB* uses its internal bonding topology data to prohibit the cleavage of higher-order bonds. Moreover, an automatic charge identification routine based on partial charges calculated with the respective GFN method is used to determine the total charge of the inner region automatically.

2.3 Jacobian

While the ONIOM single-point energy can be evaluated directly using eqn (1), structure optimizations and frequency calculations



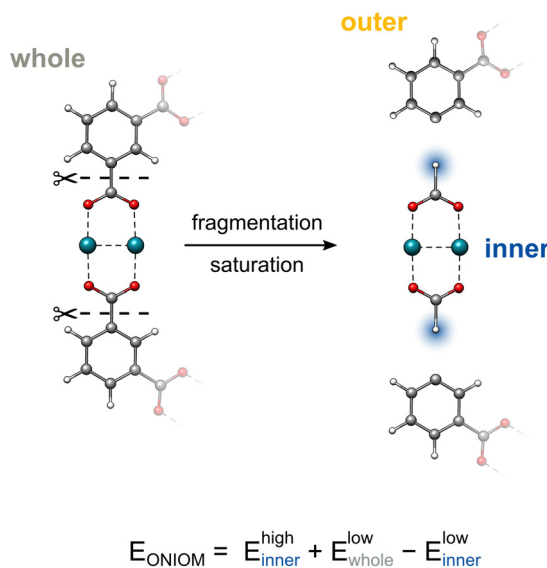


Fig. 1 The fragmentation and subsequent saturation procedures within the ONIOM framework. Capping hydrogen atoms are highlighted in blue.

require energy derivatives, such as gradients or the Hessian, that need additional treatment. The major complication emerges from the forces introduced by the artificial capping atoms that have to be reassigned accurately to the corresponding real atoms. For this purpose, the Jacobian matrix is used, which is defined as

$$J(\vec{R}_{\text{inner}}; \vec{R}_{\text{whole}}) = \frac{\delta \vec{R}_{\text{inner}}}{\delta \vec{R}_{\text{whole}}} \quad (4)$$

where R_{inner} denotes the coordinates of the inner region atoms, while R_{whole} are the coordinates of the atoms of the entire system. Taking this correction factor into consideration, the final expression for the ONIOM gradients for the two-layer interpolation is derived from the gradients calculated with the high- ($\vec{g}_{\text{inner}}^{\text{high}}$) and low-level ($\vec{g}_{\text{whole}}^{\text{low}}$, $\vec{g}_{\text{inner}}^{\text{low}}$) methods and can be written as

$$\vec{g}_{\text{ONIOM}} = \vec{g}_{\text{whole}}^{\text{low}} - \vec{g}_{\text{inner}}^{\text{low}} J(\vec{R}_{\text{inner}}; \vec{R}_{\text{whole}}) + \vec{g}_{\text{inner}}^{\text{high}} J(\vec{R}_{\text{inner}}; \vec{R}_{\text{whole}}) \quad (5)$$

The formation of the Jacobian matrix requires the differentiation of eqn (3) with respect to the real coordinates (\vec{R}_{whole}).

2.4 Implementation and availability

The ONIOM scheme implemented in the *xtb*^{22,57} program package is invoked with one simple command line instruction and can be used as a standalone program with any GFN method combination. Further, it can be interfaced with ORCA or TURBOMOLE to combine DFT/WFT with the GFN methods. The application guideline and installation instructions for the *xtb* program can be found at the <https://xtb-docs.readthedocs.io/en/latest/onion.htmlxtb-docspage>.

3 Computational details

All GFN1-xTB, GFN2-xTB, GFN-FF, and ONIOM calculations were performed with the *xtb* 6.6.0 program package. DFT computations,

including also the DFT part for the ONIOM scheme executed and processed by *xtb*, were performed with TURBOMOLE 7.5.1 or 7.6 except for the solvent clusters where ORCA 5.0.3 was employed. If not stated otherwise, the GBSA⁵⁸ (SQM, FF) (*xtb*, toluene), COSMO^{59,60} (TURBOMOLE, toluene), and CPCM^{61,62} (ORCA, DMSO) implicit solvation models were used and will be discussed in more detail in Section 4.2.

All DFT calculations employ Ahlrichs' def2 Gaussian type atomic orbital basis sets⁶³ and some modified variants developed in the framework of the respective DFT-3c composite methods PBEh-3c⁶⁴ (def2-msVP), B97-3c⁶⁵ (def-mTZVP), and r²SCAN-3c⁶⁶ (def-mTZVPP). Matching def2 effective core potentials⁶⁷ were used throughout. If not stated otherwise, the default calculation settings and convergence criteria of the respective codes were applied including the use of the resolution of the identity (RI) approximation with matching auxiliary basis sets.⁶⁸ The D4^{69–71} London dispersion correction was used throughout.

The systematic workflow for locating transition states was adopted from the work of Dohm *et al.*⁷² The double-ended Growing-String Method (GSM) by Zimmerman *et al.* was used to refine reaction paths^{73–75} at the GFN2-xTB potential energy surface (PES). The resulting saddle points were further optimized with corresponding density functionals to obtain final transition state geometries. All calculations were executed on an Intel® Xeon® CPU E5-2660 v4 @ 2.00 GHz machine.

4 Results and discussion

In the following, the application of our general ONIOM scheme implementation in *xtb* is demonstrated for selected showcases ranging from geometry optimizations of MOF cutouts, and explicit solvation of transition metal complexes to reaction mechanism exploration at metal–organic polyhedra.

4.1 Molecular structures

A great benefit of multi-layer approaches such as ONIOM is the drastic reduction of computation time compared to a full DFT or WFT approach. This is especially important for geometry optimizations that often represent one of the most time-consuming tasks in computational chemistry workflows.

As a demonstration, the following examples show the use of our implementation for geometry optimizations of challenging metal–organic systems. To allow for a fair assessment of the ONIOM results, the showcase systems were selected to still be treatable at a reasonable DFT level. Thus, a direct comparison of the multi-layer combinations and full DFT is possible. As the size of the investigated systems limits the choice of suitable methods, the TPSS⁷⁶ functional in combination with the def2-SVP basis set was chosen as the DFT approach. Nevertheless, employing the ONIOM scheme would allow for the treatment of much larger structures, where a full DFT treatment even at this low level would be unfeasible.

As a first example, a 484 atoms large cutout of the prominent zirconium-based UiO-66 MOF, synthesized by Cavka *et al.*,⁷⁷

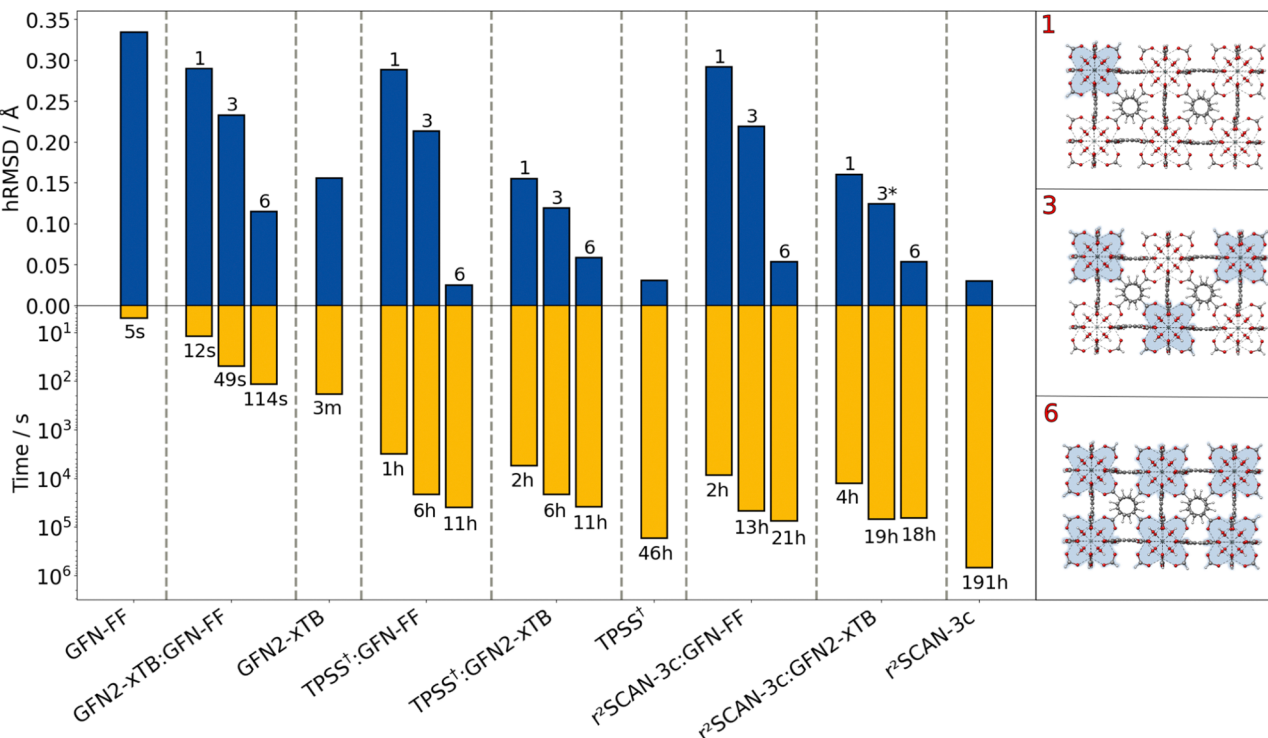


Fig. 2 hRMSD (vs. X-Ray reference) and wall time values (14 cores) for the geometry optimization of the UiO-66 polyhedron. 1, 3, and 6 are the numbers of the metal clusters included in the inner region, which is highlighted in blue. TPSS[†] = TPSS-D4/def2-SVP. *Extended number of optimization cycles due to the convergence issue.

was examined. Various combinations of GFN and DFT methods were tested within the ONIOM scheme (Fig. 2) for optimizing the geometry. For the ONIOM calculations, the Zr-containing nodes were treated with the high-level method. The resulting method combinations are denoted as “ONIOM(high-level method:low-level method)” in the following. The influence of the inner region size on the ONIOM performance was tested by including one, three, and six Zr nodes. In general, the included Zr nodes were treated as one single extended inner region, not as separated subregions. As a measure of structural quality, the heavy-atom root-mean-square deviation (hRMSD) from the crystal structure is used.

Despite having the largest deviation from the reference, the atomistic GFN-FF is highly efficient in terms of computational timings (5 s). It performs well for the purely organic linker and is still reasonable for the Zr-moiety. The semi-empirical GFN2-xTB shows an improved structure compared to GFN-FF by still remaining computationally efficient (3 min). Applying the ONIOM(GFN2-xTB:GFN-FF) scheme yields a better hRMSD compared to a full GFN-FF optimization already with only one Zr moiety in the inner region. By extending the GFN2-xTB region to the other Zr moieties, the geometry can be improved systematically while still being computationally very efficient. Applying GFN2-xTB to each of the six Zr nodes leads to a slightly lower hRMSD compared to the full GFN2-xTB optimization. The combination of GFN2-xTB for the metal-containing moieties and GFN-FF for the purely organic linker matches the strengths of both methods and yields a very reasonable geometry within seconds up to a few minutes.

The overall lowest hRMSDs are observed for the two DFT methods (TPSS and r²SCAN-3c), but with these methods, the geometry optimization takes several hours up to more than a week for r²SCAN-3c. The combination of DFT methods and GFN-FF does not yield improved hRMSDs over the ONIOM(GFN2-xTB:GFN-FF) approach for the inclusion of one or three Zr nodes. This may be due to asymmetrical distortions of the overall structure which is not the case when six nodes are included in the inner region. Then, the ONIOM(DFT:GFN-FF) combination yields excellent agreement with the reference and the full-DFT treatments. The computation time is reduced from 46 to only 11 hours at no loss in accuracy in case of employing TPSS. The reduction in computational time is even larger for the ONIOM(r²SCAN-3c:GFN-FF) combination (191 hours to 21 hours). Accordingly, the ONIOM approach can save days to weeks of computation time at no relevant loss in accuracy. Noteworthy here is the lower computational time for the inner region including six nodes with the ONIOM(r²SCAN-3c:GFN2-xTB) scheme compared to that including three nodes. This can be explained due to faster convergence of the geometries resulting from the consistent DFT treatment of the zirconium-centered moieties.

Another possible use case of our implementation is the modeling of explicit solvation. If an implicit solvation model becomes insufficient to describe the solvent effect, it is necessary to include explicit solvent molecules which can increase the computational costs tremendously. To still include a sufficient amount of explicit solvents to describe the system accurately, the ONIOM scheme can be used to employ a DFT or WFT

method for the solute and a GFN method for the solvent. In this case, no covalent bonds are broken, which renders the GFN methods specifically suitable as they are designed to reproduce non-covalent interactions accurately.

As an example, the Bis(cyclopentadienyl)silylniobium complex $[\text{Cp}_2 \text{Nb}(\text{H})_2 (\text{SiCl}^i\text{Pr}_2)]^{78}$ (Fig. 3A) was solvated with 20 DMSO molecules using the quantum-cluster-growth (QCG) algorithm.^{30,79} This transition metal complex has previously proven to be a specifically difficult case for common semi-empirical methods in the TMG145 benchmark study.¹⁹ The solvated complex was optimized at three different levels, TPSS-D4(CPCM)/def2-SVP (Fig. 3C), GFN2-xTB(ALPB), and ONIOM(TPSS-D4/def2-SVP:GFN2-xTB(ALPB)). In the ONIOM scheme, the bis(cyclopentadienyl)silylniobium complex was chosen as the inner region. A comparison of the cutout solute geometry optimized within the ONIOM scheme and pure GFN2-xTB is shown in Fig. 3B. Optimizing the explicitly solvated complex with TPSS-D4/def2-SVP retains the major structure motif of the Bis(cyclopentadienyl)silylniobium complex with respect to the gas-phase TPSSh⁸⁰-D3(BJ)-ATM reference structure.¹⁹ Using GFN2-xTB for optimizing the whole cluster yields a qualitatively wrong, distorted structure with an RMSD of 0.26 Å of the cutout solute in respect to the fully DFT optimized geometry. Thereby, a hapticropic shift of the cyclopentadienyl ligands occurs and the

symmetric coordination of the terminal hydride ligands is distorted. Accordingly, GFN2-xTB is, similar to other semi-empirical and Force Field methods,¹⁹ not able to describe this complex system accurately. Applying the ONIOM(TPSS-D4/def2-SVP:GFN2-xTB) scheme instead yields the correct structure in excellent agreement with the full DFT optimization (RMSD of 0.01 Å) at a fraction of computational costs (59 min vs. 48 h 58 min). Despite the good performance of the ONIOM scheme demonstrated for this example, electrostatic embedding may enhance the results for cases with highly polar environments showing strong charge-dependent interactions. Nevertheless, the appropriate choice of the ONIOM boundary may reduce errors in this respect.

4.2 Electronic energies

Another key ability of the ONIOM scheme is the calculation of energies for extended structures. This is specifically useful for, *e.g.*, reaction mechanism elucidation, where the chemical transformation is typically occurring at a relatively small reactive site.

As a first example, we discuss the Rh-functionalized metal-organic cuboctahedron illustrated in Fig. 4. In the following, it is referred to as DALTES⁸¹ in correspondence with its reference code from the Cambridge Structural Database (CSD).⁸²

Herein, we consider the cyanosilylation reaction facilitated by the dirhodium paddle-wheel nodes (Fig. 5A). The proposed mechanism depicted in Fig. 5B was adapted from Zhang *et al.*⁸³ The first step is the coordination of an aldehyde substrate to the open Rh sites of DALTES, which is followed by the nucleophilic addition of the isomerized trimethylsilyl cyanide (iso-TMSCN) to the activated carbonyl compound. Afterwards, the trimethylsilyl group isomerizes into the product which is

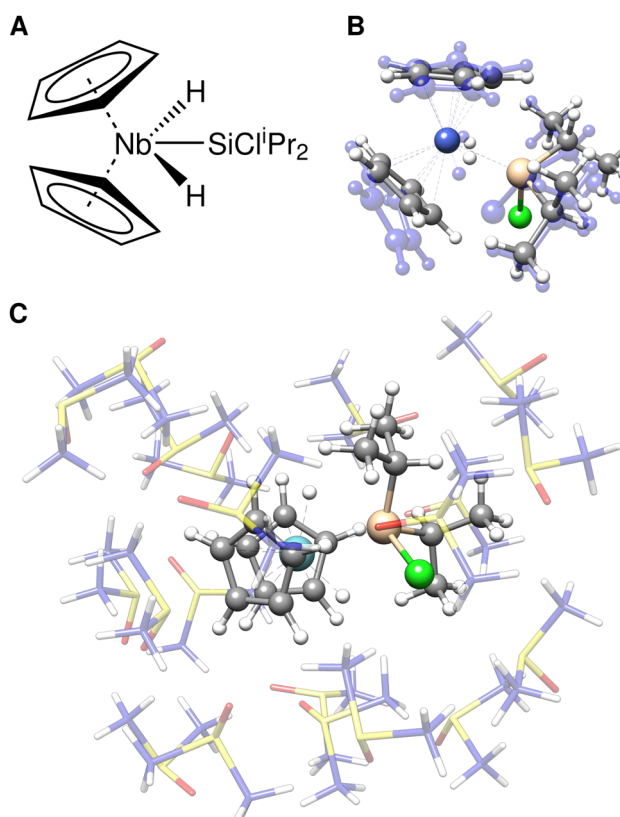


Fig. 3 (A) Lewis structure depiction of $[\text{Cp}_2 \text{Nb}(\text{H})_2 (\text{SiCl}^i\text{Pr}_2)]$. (B) structure overlay of the full GFN2-xTB (blue) and TPSS-D4/def2-SVP (color-coded) optimized structures. DMSO molecules are removed for clarification. (C) TPSS-D4/def2-SVP optimized geometry of $[\text{Cp}_2 \text{Nb}(\text{H})_2 (\text{SiCl}^i\text{Pr}_2)]$ dissolved by 20 DMSO molecules.

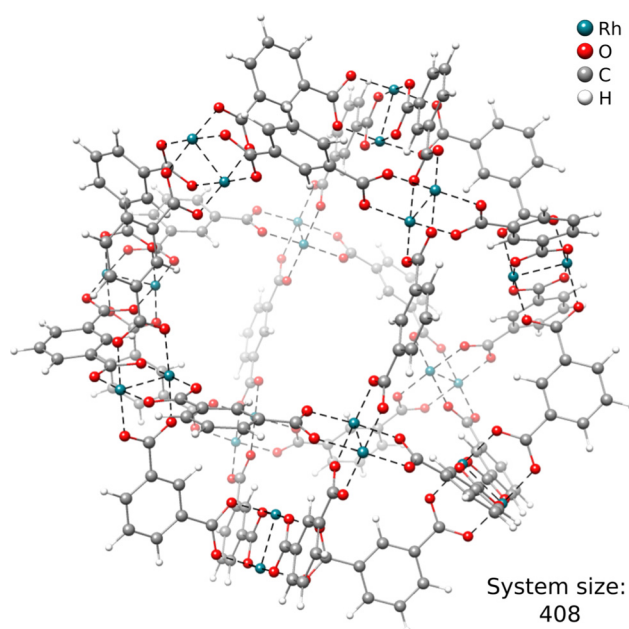


Fig. 4 The molecular structure of the DALTES metal-organic polyhedron.



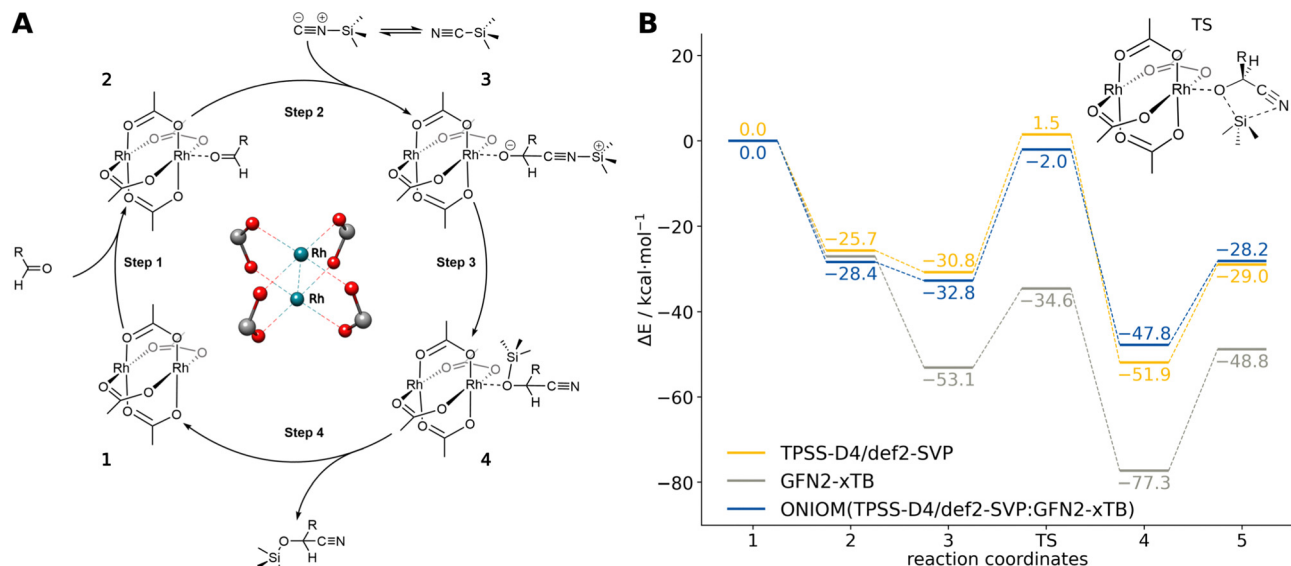


Fig. 5 (A) Schematic reaction mechanism of the cyanosilylation at an Rh-based paddle-wheel motif of the DALTES MOP. (B) The relative potential energy curve of the cyanosilylation reaction computed with TPSS-D4/def2-SVP, GFN2-xTB, and their ONIOM(TPSS-D4/def2-SVP:GFN2-xTB) combination for the TPSS-D4/def2-SVP optimized geometries implicitly solvated in toluene.

the rate-determining step of the catalytic reaction. Finally, the produced cyanohydrin derivative is cleaved from the metal cluster of the catalysts. To validate the ONIOM approach, a full quantum mechanical reference energy profile was calculated. Due to the size of the investigated system (404 atoms), the choice of the reference method was again limited to the (*meta*-) GGA/DZ level. Accordingly, the TPSS-D4/def2-SVP level with COSMO implicit solvation was chosen as a reference and QM component in the ONIOM approach. The energy profile of the catalytic cycle was then recomputed at the GFN2-xTB and ONIOM(TPSS(COSMO):GFN2-xTB(ddCOSMO)) level (Fig. 5). For the ONIOM scheme, only the respective dimetal node involved in the cyanosilylation and the corresponding reactants were included in the inner region.

The semi-empirical GFN2-xTB energy profile qualitatively agrees with the full-DFT results but the relative energies differ by up to 35 kcal mol⁻¹. Applying the ONIOM approach instead yields very good agreement with the TPSS-D4/def2-SVP reference energies, only varying by 1–3 kcal mol⁻¹. Accordingly, the ONIOM scheme can be used to effectively converge the results by combining GFN2-xTB with any suitable DFT method of choice. Using ONIOM reduces the average computational wall time of the energy evaluations from 30 minutes to only 40 seconds. This allows choosing a significantly more accurate method in the inner region that would be unfeasible in a full DFT approach. Similar results are obtained for other methods combinations such as ONIOM(*r*²SCAN-3c:GFN2-xTB) and ONIOM(ω B97X-3c⁸⁴:GFN2-xTB) (see ESI[†]).

An even more challenging system is the recently synthesized porphyrin-based macromolecular spoked-wheel complex by Majewski *et al.*⁸⁵ illustrated in Fig. 6. Its size of 870 atoms renders most conventional DFT methods unfeasible, but the bond formations at the rim of the spoked-wheel complex can be

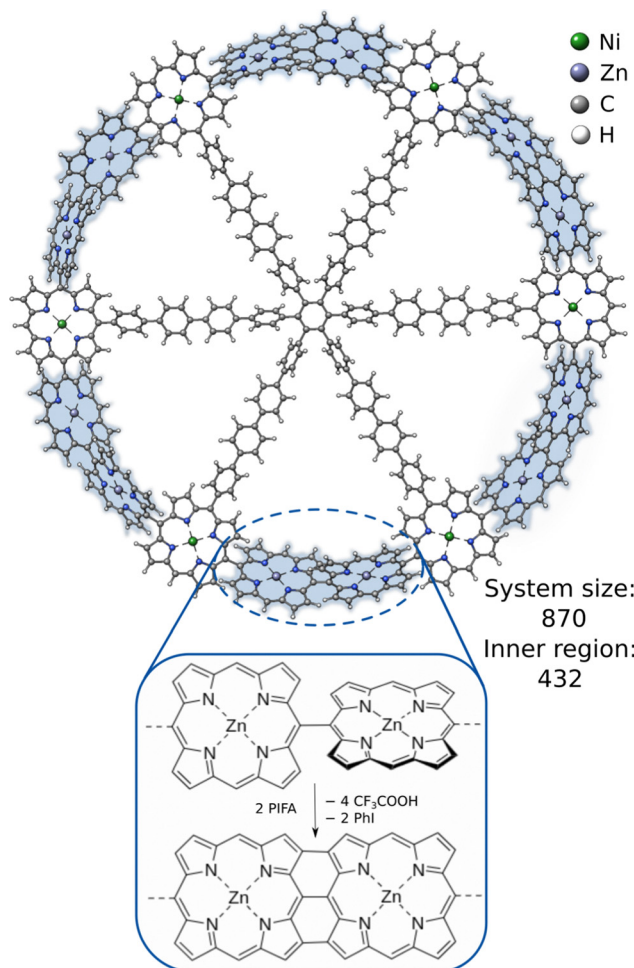


Fig. 6 The molecular structure of the 5,15-linked porphyrin nanoring and the fusion reaction between its Zn-functionalized porphyrin units.

Table 1 The C–C coupling reaction energies of the 5,15-linked porphyrin nanoring implicitly solvated in toluene (ddCOSMO) and calculated for the corresponding molecular geometries optimized at the same levels of theory with the corresponding wall time (28 cores) values for the self-consistent field (SCF) energy calculation. TPSS[†] = TPSS-D4/def2-SVP

Methods	$\Delta E/\text{kcal mol}^{-1}$	SCF time
ONIOM(TPSS [†] :GFN2-xTB)	−44.9	25 m
GFN2-xTB	−34.9	36 s
ONIOM(GFN2-xTB:GFN-FF)	−24.4	4 s
ONIOM(TPSS [†] :GFN1-xTB)	−47.0	24 m
GFN1-xTB	−37.6	39 s
ONIOM(GFN1-xTB:GFN-FF)	−26.6	4 s
ONIOM(TPSS [†] :GFN-FF)	−35.3	15 m
GFN-FF	172.6	0.4 s

computed employing DFT within the ONIOM approach. The rim of the spoked-wheel complex consists of 18 5,15-linked porphyrin units coordinated by Zn(II) or Ni(II) ions. By the addition of bis(trifluoroacetoxy)iodobenzene (PIFA), the meso-meso coupled Zn–porphyrin rings can be fused further forming a nanobelト involving three-fold single bond coupled Zn–porphyrin units. The corresponding reaction energy of this coupling reaction was computed including the Zinc-functionalized porphyrin rings in the inner region with 432 atoms. The obtained reaction energies are shown in Table 1. The reference method (ONIOM(TPSS:GFN2-xTB(GBSA))) yields an overall reaction energy of $−44.9 \text{ kcal mol}^{-1}$. GFN2-xTB and GFN1-xTB yield reasonable reaction energies of $−37.6$ and $−34.9 \text{ kcal mol}^{-1}$, respectively, and show the qualitatively right trend. Using only GFN-FF yields a much too high, qualitatively wrong interaction energy. Combing it with GFN n -xTB within the ONIOM scheme can reduce this error drastically and gives a qualitatively correct behavior. These results show that it is possible to get good and fast results with the ONIOM(GFN n -xTB:GFN-FF) scheme and that, if more accurate results are required for such large systems, ONIOM(DFT:GFN) can be a valuable tool as full DFT calculations are yet too costly.

5 Conclusions

In the course of this work, the subtractive ONIOM scheme was implemented into the free, open-source *xtb* software package. Furthermore, several new implementation-specific features such as an automatic charge and topology handling were introduced. The utility of the ONIOM scheme in combination with the GFN family of semi-empirical and force-field methods was demonstrated exemplary for geometry optimizations and reaction energy evaluations of large metal–organic systems. Various combinations of DFT and GFN methods were tested using the interface of *xtb* to the popular quantum chemistry packages TURBOMOLE and ORCA.

It was shown that the ONIOM approach can be utilized to clearly improve on the already reasonable results of the GFN methods for challenging systems containing many transition metal atoms. By matching the strengths of the GFN methods and DFT, even critical cases that require a highly accurate quantum mechanical description can be treated. Accordingly,

we demonstrated that by using the ONIOM framework in *xtb*, DFT quality reaction energies and molecular structures can be obtained at a fraction of the computational costs of conventional DFT. This allows also the use of computationally more expensive and more accurate DFT methods. The efficient, robust, and easy-to-use implementation of the ONIOM scheme into *xtb* opens up new possibilities with regard to the treatment of very large systems containing a variety of elements across the periodic table.

Conflicts of interest

There are no conflicts to declare.

Acknowledgements

The German Science Foundation (DFG) is gratefully acknowledged for financial support through a Gottfried Wilhelm Leibniz prize to S. G. and the Merck KGaA. Further, S. G. and M. B. gratefully acknowledge financial support of the Max Planck Society through the Max Planck fellow program. Open Access funding provided by the Max Planck Society.

References

- 1 I. V. Kolesnichenko and E. V. Anslyn, *Chem. Soc. Rev.*, 2017, **46**, 2385–2390.
- 2 M. S. Gordon, J. M. Mullin, S. R. Pruitt, L. B. Roskop, L. V. Slipchenko and J. A. Boatz, *J. Phys. Chem. B*, 2009, **113**, 9646–9663.
- 3 S. Kobayashi and H. Uyama, *Macromol. Chem. Phys.*, 2003, **204**, 235–256.
- 4 R. Morris, K. A. Black and E. J. Stollar, *Essays Biochem.*, 2022, **66**, 255–285.
- 5 A. C. Ghosh, A. Legrand, R. Rajapaksha, G. A. Craig, C. Sassoye, G. Balázs, D. Farrusseng, S. Furukawa, J. Canivet and F. M. Wisser, *J. Am. Chem. Soc.*, 2022, **144**, 3626–3636.
- 6 D. Fujita, Y. Ueda, S. Sato, N. Mizuno, T. Kumasaka and M. Fujita, *Nature*, 2016, **540**, 563–566.
- 7 F. Lancia, A. Ryabchun and N. Katsonis, *Nat. Rev. Chem.*, 2019, **3**, 536–551.
- 8 J. Kohn, S. Spicher, M. Bursch and S. Grimme, *Chem. Commun.*, 2021, **58**, 258–261.
- 9 S. Mallakpour, E. Nikkhoo and C. M. Hussain, *Coord. Chem. Rev.*, 2022, **451**, 214262.
- 10 J. Cao, X. Li and H. Tian, *Curr. Med. Chem.*, 2019, **27**, 5949–5969.
- 11 R. F. Mendes and F. A. A. Paz, *Inorg. Chem. Front.*, 2015, **2**, 495–509.
- 12 A. Bavykina, N. Kolobov, I. S. Khan, J. A. Bau, A. Ramirez and J. Gascon, *Chem. Rev.*, 2020, **120**, 8468–8535.
- 13 M. L. Hu, V. Safarifard, E. Doustkhah, S. Rostamnia, A. Morsali, N. Nouruzi, S. Beheshti and K. Akhbari, *Microporous Mesoporous Mater.*, 2018, **256**, 111–127.

14 S. Spicher, M. Bursch and S. Grimme, *J. Phys. Chem. C*, 2020, **124**, 27529–27541.

15 A. Lledós, *Eur. J. Inorg. Chem.*, 2021, 2547–2555.

16 Y. P. Chin, N. W. See, I. D. Jenkins and E. H. Krenske, *Org. Biomol. Chem.*, 2022, **20**, 2028–2042.

17 T. S. Hofer, *Front. Chem.*, 2013, **1**, 6.

18 W. Thiel, *Wiley Interdiscip. Rev.: Comput. Mol. Sci.*, 2014, **4**, 145–157.

19 M. Bursch, H. Neugebauer and S. Grimme, *Angew. Chem., Int. Ed.*, 2019, **131**, 11195–11204.

20 S. Piana, P. Robustelli, D. Tan, S. Chen and D. E. Shaw, *J. Chem. Theory Comput.*, 2020, **16**, 2494–2507.

21 F. Spiegelman, N. Tarrat, J. Cuny, L. Dontot, E. Posenitskiy, C. Martí, A. Simon and M. Rapacioli, *Adv. Phys. X*, 2020, **5**, 1710252.

22 C. Bannwarth, E. Caldeweyher, S. Ehlert, A. Hansen, P. Pracht, J. Seibert, S. Spicher and S. Grimme, *Wiley Interdiscip. Rev.: Comput. Mol. Sci.*, 2021, **11**, e1493.

23 S. Grimme, C. Bannwarth and P. Shushkov, *J. Chem. Theory Comput.*, 2017, **13**, 1989–2009.

24 C. Bannwarth, S. Ehlert and S. Grimme, *J. Chem. Theory Comput.*, 2019, **15**, 1652–1671.

25 S. Spicher and S. Grimme, *Angew. Chem., Int. Ed.*, 2020, **59**, 15665–15673.

26 S. Grimme, F. Bohle, A. Hansen, P. Pracht, S. Spicher and M. Stahn, *J. Phys. Chem. A*, 2021, **125**, 4039–4054.

27 Y. Q. Chen, Y. J. Sheng, Y. Q. Ma and H. M. Ding, *Phys. Chem. Chem. Phys.*, 2022, **24**, 14339–14347.

28 P. Pracht, F. Bohle and S. Grimme, *Phys. Chem. Chem. Phys.*, 2020, **22**, 7169–7192.

29 S. Grimme, F. Bohle, A. Hansen, P. Pracht, S. Spicher and M. Stahn, *J. Phys. Chem. A*, 2021, **125**, 4039–4054.

30 C. Plett and S. Grimme, *Angew. Chem., Int. Ed.*, 2023, **62**, e202214477.

31 M. Bursch, J.-M. Mewes, A. Hansen and S. Grimme, *Angew. Chem., Int. Ed.*, 2022, **61**, e202205735.

32 L. W. Chung, W. M. C. Sameera, R. Ramozzi, A. J. Page, M. Hatanaka, G. P. Petrova, T. V. Harris, X. Li, Z. Ke, F. Liu, H.-B. Li, L. Ding and K. Morokuma, *Chem. Rev.*, 2015, **115**, 5678–5796.

33 N. Koga, R. Koga, G. Liu, J. Castellanos, G. T. Montelione and D. Baker, *Nat. Commun.*, 2021, **12**, 1–12.

34 A. Galan and P. Ballester, *Chem. Soc. Rev.*, 2016, **45**, 1720–1737.

35 G. Olivo, G. Capocasa, D. Del Giudice, O. Lanzalunga and S. Di Stefano, *Chem. Soc. Rev.*, 2021, **50**, 7681–7724.

36 J. Yang, L. Zhao, Y. Sun and H. Sun, *ChemPhysChem*, 2009, **10**, 946–953.

37 M. Ruan, H. Hou, B. Wang, W. Li, Y. Chen, X. Deng and X. Zuo, *Theor. Chem. Acc.*, 2018, **137**, 1–10.

38 I. Geronimo and P. Paneth, *Phys. Chem. Chem. Phys.*, 2014, **16**, 13889–13899.

39 C. E. Tzeliou, M. A. Mermigki and D. Tzeli, *Molecules*, 2022, **27**, 2660.

40 F. Maseras and K. Morokuma, *J. Comput. Chem.*, 1995, **16**, 1170–1179.

41 A. Fu, W. Meng, H. Li, J. Nie and J. A. Ma, *Org. Biomol. Chem.*, 2014, **12**, 1908–1918.

42 G. Mora, B. Deschamps, S. Van Zutphen, X. F. Le Goff, L. Ricard and P. Le Floch, *Organometallics*, 2007, **26**, 1846–1855.

43 Y. Li, W. Guo, W. Fan, S. Yuan, J. Li, J. Wang, H. Jiao and T. Tatsumi, *J. Mol. Catal. A: Chem.*, 2011, **338**, 24–32.

44 J. Aezáć and J. J. Stewart, *J. Chem. Phys.*, 2023, **158**, 44118.

45 S. Schmitz, J. Seibert, K. Ostermeir, A. Hansen, A. H. Göller and S. Grimme, *J. Phys. Chem. B*, 2020, **124**, 3636–3646.

46 M. Bursch, A. Hansen and S. Grimme, *Inorg. Chem.*, 2017, **56**, 12485–12491.

47 F. Neese and J. Wiley, *Wiley Interdiscip. Rev.: Comput. Mol. Sci.*, 2012, **2**, 73–78.

48 F. Neese, *Wiley Interdiscip. Rev.: Comput. Mol. Sci.*, 2022, **12**, e1606.

49 TURBOMOLE V7.6 2021, a development of University of Karlsruhe and Forschungszentrum Karlsruhe GmbH, 1989–2007, TURBOMOLE GmbH, since 2007; available from <http://www.turbomole.com>.

50 R. Ahlrichs, M. Bär, M. Häser, H. Horn and C. Kölmel, *Chem. Phys. Lett.*, 1989, **162**, 165–169.

51 L. Bösel, M. Thürlemann and S. Riniker, *J. Chem. Theory Comput.*, 2021, **17**, 2641–2658.

52 G. A. Bramley, O. T. Beynon, P. V. Stishenko and A. J. Logsdail, *Phys. Chem. Chem. Phys.*, 2023, **25**, 6562–6585.

53 H. Lin and D. G. Truhlar, *Theor. Chem. Acc.*, 2007, **117**, 185–199.

54 M. J. Field, P. A. Bash and M. Karplus, *J. Comput. Chem.*, 1990, **11**, 700–733.

55 H. M. Senn and W. Thiel, *Top. Curr. Chem.*, 2007, **268**, 173–290.

56 G. Tóth and G. Náray-Szabó, *J. Chem. Phys.*, 1994, **100**, 3742–3746.

57 Semiempirical Extended Tight-Binding Program Package, 2023, <https://github.com/grimme-lab/xtb>.

58 S. Ehlert, M. Stahn, S. Spicher and S. Grimme, *J. Chem. Theory Comput.*, 2021, **17**, 4250–4261.

59 A. Klamt and G. Schüürmann, *J. Chem. Soc., Perkin Trans. 2*, 1993, 799–805.

60 A. Klamt, *Wiley Interdiscip. Rev.: Comput. Mol. Sci.*, 2011, **1**, 699–709.

61 V. Barone and M. Cossi, *J. Phys. Chem. A*, 1998, **102**, 1995–2001.

62 M. Garcia-Ratés and F. Neese, *J. Comput. Chem.*, 2020, **41**, 922–939.

63 F. Weigend and R. Ahlrichs, *Phys. Chem. Chem. Phys.*, 2005, **7**, 3297–3305.

64 S. Grimme, J. G. Brandenburg, C. Bannwarth and A. Hansen, *J. Chem. Phys.*, 2015, **143**, 054107.

65 J. G. Brandenburg, C. Bannwarth, A. Hansen and S. Grimme, *J. Chem. Phys.*, 2018, **148**, 064104.

66 S. Grimme, A. Hansen, S. Ehlert and J. M. Mewes, *J. Chem. Phys.*, 2021, **154**, 064103.

67 D. Andrae, U. Häußermann, M. Dolg, H. Stoll and H. Preuß, *Theor. Chim. Acta*, 1990, **77**, 123–141.



68 F. Weigend, *Phys. Chem. Chem. Phys.*, 2006, **8**, 1057–1065.

69 E. Caldeweyher, C. Bannwarth and S. Grimme, *J. Chem. Phys.*, 2017, **147**, 034112.

70 E. Caldeweyher, S. Ehlert, A. Hansen, H. Neugebauer, S. Spicher, C. Bannwarth and S. Grimme, *J. Chem. Phys.*, 2019, **150**, 154122.

71 E. Caldeweyher, J. M. Mewes, S. Ehlert and S. Grimme, *Phys. Chem. Chem. Phys.*, 2020, **22**, 8499–8512.

72 S. Dohm, M. Bursch, A. Hansen and S. Grimme, *J. Chem. Theory Comput.*, 2020, **16**, 8.

73 P. M. Zimmerman, *J. Chem. Phys.*, 2013, **138**, 184102.

74 P. M. Zimmerman, *J. Chem. Theory Comput.*, 2013, **9**, 3043–3050.

75 M. Jafari and P. M. Zimmerman, *J. Comput. Chem.*, 2017, **38**, 645–658.

76 J. Tao, J. P. Perdew, V. N. Staroverov and G. E. Scuseria, *Phys. Rev. Lett.*, 2003, **91**, 146401.

77 J. H. Cavka, S. Jakobsen, U. Olsbye, N. Guillou, C. Lamberti, S. Bordiga and K. P. Lillerud, *J. Am. Chem. Soc.*, 2008, **130**, 13850–13851.

78 K. Y. Dorogov, A. V. Churakov, L. G. Kuzmina, J. A. Howard and G. I. Nikonorov, *Eur. J. Inorg. Chem.*, 2004, 771–775.

79 S. Spicher, C. Plett, P. Pracht, A. Hansen and S. Grimme, *J. Chem. Theory Comput.*, 2022, **18**, 3174–3189.

80 J. P. Perdew, J. Tao, V. N. Staroverov and G. E. Scuseria, *J. Chem. Phys.*, 2004, **120**, 6898.

81 S. Furukawa, N. Horike, M. Kondo, Y. Hijikata, A. Carné Sánchez, P. Larpent, N. Louvain, S. Diring, H. Sato and R. Matsuda, *et al.*, *Inorg. Chem.*, 2016, **55**, 10843–10846.

82 C. R. Groom, I. J. Bruno, M. P. Lightfoot and S. C. Ward, *Acta Crystallogr., Sect. B: Struct. Sci., Cryst. Eng. Mater.*, 2016, **72**, 171–179.

83 Z. Zhang, J. Chen, Z. Bao, G. Chang, H. Xing and Q. Ren, *RSC Adv.*, 2015, **5**, 79355–79360.

84 M. Müller, A. Hansen and S. Grimme, *J. Chem. Phys.*, 2023, **158**, 14103.

85 M. A. Majewski, W. Stawski, J. M. V. Raden, M. Clarke, J. Hart, J. N. O'Shea, A. Saywell and H. L. Anderson, *Angew. Chem., Int. Ed.*, 2023, **62**, e202302114.

